NUMERICAL LINEAR ALGEBRA WITH APPLICATIONS
Numer. Linear Algebra Appl. 2012; **19**:153–173
Published online 27 September 2010 in Wiley Online Library (wileyonlinelibrary.com). DOI: 10.1002/nla.750

Coupled segmentation and denoising/deblurring models for hyperspectral material identification

Fang Li[1], Michael K. Ng[2] and Robert J. Plemmons[3,*,†]

[1]*Department of Mathematics, East China Normal University, Shanghai 200062, People's Republic of China*
[2]*Centre for Mathematical Imaging and Vision and Department of Mathematics, Hong Kong Baptist University Kowloon Tong, Hong Kong, People's Republic of China*
[3]*Department of Mathematics and Computer Science, Wake Forest University, Winston-Salem, NC 27106, U.S.A.*

SUMMARY

A crucial aspect of spectral image analysis is the identification of the materials present in the object or scene being imaged and to quantify their abundance in the mixture. An increasingly useful approach to extracting such underlying structure is to employ image classification and object identification techniques to compressively represent the original data cubes by a set of spatially orthogonal bases and a set of spectral signatures. Owing to the increasing quantity of data usually encountered in hyperspectral data sets, effective data compressive representation is an important consideration, and noise and blur can present data analysis problems. In this paper, we develop image segmentation methods for hyperspectral space object material identification. We also couple the segmentation with a hyperspectral image data denoising/deblurring model and propose this method as an alternative to a tensor factorization methods proposed recently for space object material identification. The model provides the segmentation result and the restored image simultaneously. Numerical results show the effectiveness of our proposed combined model in hyperspectral material identification. Copyright © 2010 John Wiley & Sons, Ltd.

Received 14 April 2010; Revised 26 July 2010; Accepted 8 August 2010

KEY WORDS: hyperspectral image analysis; segmentation; denoising; deblurring; compressive representation; tensors

1. INTRODUCTION

Hyperspectral remote sensing technology allows one to capture images using a range of spectra from ultraviolet to visible to infrared. Multiple images of a scene or object are created using light from different parts of the spectrum. These hyperspectral images can be used, for example, to detect and identify objects at a distance, to identify surface minerals, objects and buildings from space, and to enable space object identification (SOI) from the ground. In this particular study within the domain of SOI, we concentrate on hyperspectral image deblurring, segmentation, and object material identification.

*Correspondence to: Robert J. Plemmons, Department of Mathematics and Computer Science, Wake Forest University, Winston-Salem, NC 27106, U.S.A.
†E-mail: plemmons@wfu.edu

Three major objectives in processing hyperspectral image data of an object (target) are data compressive representation, spectral signature identification of constituent materials, and determination of their corresponding fractional abundances. Note that a hyperspectral image can be considered as a 3D tensor, e.g. [1]. Zhang *et al.* [2] have proposed a novel approach to processing hyperspectral data (tensors) using nonnegative tensor factorization (NTF) for 3-D arrays, which reduces a large tensor into three nonnegative factor matrices, whose Khatri–Rao product approximates the original tensor, see e.g. [3]. This approach preserves physical characteristics of the data such as nonnegativity and is a natural extension of nonnegative least-squares approximate nonnegative matrix factorization (NMF), see e.g. [4]. However, the use of NTF was only partially successful in [2]. Hyperspectral data are typically noisy and suffer from both spatial and spectral blurring, e.g. [5–8]. Those problems were also reported in [2]. Also, analyzing tensors is challenging. Algorithms fitting tensor models depend heavily upon the initial set-up, i.e. the number of components and the initialization of the component matrices. See the NSF Workshop report by Van Loan [1] for a discussion of tensor computations and research needed for these problems.

Here, we propose an alternative to the use of NTF for hyperspectral data analysis with space object material identification applications. We apply a coupled segmentation and deblurring model to the problem of hyperspectral material (sometimes called endmember) identification. This approach is tested with data used in [2] for SOI applications. In Section 2, a coupled segmentation and deblurring model is proposed, and the numerical implementation of the proposed method is given in Section 3. We then describe the hyperspectral data used for our numerical tests and its relationship to the SOI problem in Section 4. Numerical experiments are provided in Section 5, and some comments and open problems are given in Section 6.

2. COUPLED SEGMENTATION AND DENOISING/DEBLURRING

For multi-mode data hypercubes, the enormity of direct data storage and processing tasks is often too daunting to permit a reasonable direct computational approach. This is particularly true in the context of computing information measures for highly multi-parametric statistical distributions, and where the data are blurred and noisy across the spectral bands. A different and more practical approach in this case is the one that stresses physics in the specific sense that the underlying physical model is often based on a rather much smaller set of parameters. A powerful strategy in handling what are naively large data sets is thus to devote considerable attention to the underlying physical model and to identify the small set of parameters that can explain the underlying structure of the otherwise intractable data volume. The viability of this approach is guaranteed very generally, since physical problems of any interest very often admit a complete description in terms of a relatively small set of parameters.

An increasingly useful approach to extracting such underlying structure is to employ image segmentation and object identification techniques to compressively represent the original hyperspectral cubes by a set of spatially orthogonal bases and a set of spectral traces, i.e.

$$\mathscr{T}(x, y, \lambda) \approx \sum_i \mu_i(x, y) f_i(\lambda) \quad (x, y) \in \Omega, \tag{1}$$

where Ω is the domain of the observed hyperspectral cubes, $\mu_i(x, y)$ is a binary support function for the ith object and $f_i(\lambda)$ is the spectral trace of the ith object. This is the simpler case of assuming no overlapping between objects in the spatial dimensions, i.e. $\{\mu_i\}$ are orthogonal, but it can be extended to the mixing case by changing the range of μ_i from binary to the interval of $[0, 1]$.

Thus, we anticipate a decomposition of the data into a sum of elementary images, each corresponding, e.g., to a specific material constituent of the surface of an object which can be expected to be spatially sparse in our applications. For example, in hyperspectral imaging of satellites from the ground, the μ_i could correspond to the solar panels that are localized to certain surface regions and are thus sparse over the full 2D array and the vector $f_i(\lambda)$ could correspond to a solar panel

DOI: 10.1002/nla

material spectral signature [2]. Variational PDE methods, e.g. the Chan-Vese model [9] and its extensions [10], can be employed to segment out certain regions of a single image to identify μ_i.

However, from a practical standpoint hyperspectral data are generally noisy and blurred, especially in ground-based imaging through the atmosphere, see [5, 11, 12]. This situation can complicate any attempt to segment and analyze the data, as was observed in [2]. We first describe a denoising/deblurring model that will be used to preprocess the hyperspectral data along with segmentation.

2.1. A fast denoising/deblurring model using total variation

Digital image restoration and reconstruction play an important part in numerous areas of applied sciences such as medical and astronomical imaging, image and video coding. In our particular application, we are concerned with the degradation effects of imaging through atmospheric turbulence [13].

Assume that the observed gray scale image $I_0 : \Omega \to \mathbb{R}$ is blurred with a known point spread function (psf) h and contaminated by some noise n, that is

$$I_0(x, y) = (h * I)(x, y) + n(x, y). \tag{2}$$

We assume that h satisfies $0 \leqslant h \leqslant 1$ and $\int_\Omega h(x, y)\,\mathrm{d}x\,\mathrm{d}y = 1$. In order to recover the clean image I from I_0, a total variation regularization with ℓ_2 fit-to-data term deblurring model minimizes the following energy functional:

$$E(I) = \int_\Omega |\nabla I|\,\mathrm{d}x\,\mathrm{d}y + \gamma \int_\Omega (h * I - I_0)^2\,\mathrm{d}x\,\mathrm{d}y.$$

The first term in the right-hand side is the total variation of I. Huang *et al.* [14] proposed to introduce an auxiliary variable J, and to approximate the energy $E(I)$ by

$$E(I, J) = \int_\Omega |\nabla J|\,\mathrm{d}x\,\mathrm{d}y + \frac{1}{2\theta} \int_\Omega (I - J)^2\,\mathrm{d}x\,\mathrm{d}y + \gamma \int_\Omega (h * I - I_0)^2\,\mathrm{d}x\,\mathrm{d}y.$$

Then they solve the minimizer by an alternating minimization method: Fixing I, J can be solved by Chambolle's [15] fast dual projection method; Fixing J, I can be solved in various ways, for example using the FFT when h is spatially invariant. The overall algorithm is faster than gradient descent methods [14]. Here, θ and γ are fixed parameters defined by the user. The parameters can be determined using the strategy studied in [16].

2.2. A fuzzy piecewise constant segmentation model

Image segmentation, an important problem in image analysis, is the task of partitioning a given image into disjoint regions, such that the regions correspond to the objects in the image. There are a wide variety of approaches to the segmentation problem. Based on the Mumford–Shah [17] functional for segmentation, Chan and Vese [9] proposed a level set model for active contours to detect objects whose boundaries are not necessarily defined by a gradient.

As in the Chan-Vese model as described in [9], we assume that the image can be approximated by a piecewise constant function $\sum_{i=1}^{N} c_i \chi_i$ where χ_i is the characteristic function of set Ω_i and c_i are constants, i.e.

$$I(x, y) \approx c_i \quad (x, y) \in \Omega_i,$$

where $\{\Omega_i\}_{i=1}^N$ is a partition of the image domain Ω. Then the piecewise constant segmentation problem becomes to recover the clean image I, $c = (c_1, \ldots, c_n)$, and the partition from the observed data I_0. According to (1), we determine Ω_i and c_i to match the λth frequency image of the hyperspectral tensors as follows:

$$c_i = \begin{cases} f_i(\lambda) & (x, y) \in \Omega_i \quad \text{with } \mu_i(x, y) = 1, \\ 0 & \text{otherwise.} \end{cases}$$

DOI: 10.1002/nla

For convenience, we label the background to be one region or one material. In the following discussion, we consider a segmentation and deblurring model for the λ frequency image of the hyperspectral cubes. In Section 4, the extension of the model to the whole hyperspectral tensor with all frequencies will be considered.

Let $\partial\Omega_i$ be the boundary of region Ω_i. Let $\Gamma=\bigcup_{i=1}^{N}\partial\Omega_i$ be the segmentation boundaries of the entire image. The segmentation is usually given by minimizing the piecewise constant Mumford–Shah energy functional

$$E(c,\Gamma)=|\Gamma|+\sum_{i=1}^{N}\tau\int_{\Omega_i}(I-c_i)^2\,\mathrm{d}x\,\mathrm{d}y. \tag{3}$$

In terms of characteristic functions $\chi=(\chi_1,\ldots,\chi_N)$, where χ_i denotes the characteristic function of region Ω_i, the energy (3) can be rewritten as

$$E(c,\chi)=\sum_{i=1}^{N}\int_{\Omega}|\nabla\chi_i|\,\mathrm{d}x\,\mathrm{d}y+\sum_{i=1}^{N}\tau\int_{\Omega}(I-c_i)^2\chi_i\,\mathrm{d}x\,\mathrm{d}y. \tag{4}$$

In the last term, $\int_\Omega|\nabla\chi_i|\,\mathrm{d}x\,\mathrm{d}y$ equals the perimeter of $\partial\Omega_i$. There is a scaling of factor 2, since we add each boundary twice. For simplicity, we neglect it.

The binary-valued function χ_i gives a hard segmentation of Ω. In the following, we use a fuzzy membership function $u_i(x,y)$ to substitute for the hard membership function χ_i in (4). As a fuzzy membership function, u_i must satisfy the conditions:

$$\text{(i)}\quad 0\leqslant u_i\leqslant 1\quad\text{and}\quad\text{(ii)}\quad\sum_{i=1}^{N}u_i=1. \tag{5}$$

Then we get the constrained fuzzy piecewise constant segmentation model of minimizing energy functional

$$E(U,c)=\sum_{i=1}^{N}\int_{\Omega}|\nabla u_i|\,\mathrm{d}x\,\mathrm{d}y+\sum_{i=1}^{N}\tau\int_{\Omega}(I-c_i)^2u_i^p\,\mathrm{d}x\,\mathrm{d}y, \tag{6}$$

where p is a parameter to determine the fuzziness of segmentation and $U=(u_1,\ldots,u_N)$. We remark that larger p implies more fuzziness, and in practice we set $p=2$.

For images without noise and/or blur, the fuzzy piecewise constant segmentation model generally works quite well, e.g. [18, 19].

2.3. The combined model

Here we combine the denoising/deblurring model and the fuzzy piecewise constant segmentation model together with $p=2$ and h is a known spatial invariant blurring operator. We then obtain a coupled model for deblur and segmentation, which has to minimize

$$\begin{aligned}E(U,c,I)=&\int_{\Omega}|\nabla I|\,\mathrm{d}x\,\mathrm{d}y+\sum_{i=1}^{N}\int_{\Omega}|\nabla u_i|\,\mathrm{d}x\,\mathrm{d}y+\frac{\gamma}{2}\int_{\Omega}(h*I-I_0)^2\,\mathrm{d}x\,\mathrm{d}y\\&+\sum_{i=1}^{N}\frac{\tau}{2}\int_{\Omega}(I-c_i)^2u_i^2\,\mathrm{d}x\,\mathrm{d}y\end{aligned} \tag{7}$$

subject to constraints (i) and (ii) in (5).

Assume that the observed image $I_0\in\mathrm{BV}(\Omega)\cap L^\infty(\Omega)$ and $\alpha=\operatorname{ess\,inf}_\Omega I_0$, $\beta=\operatorname{ess\,sup}_\Omega I_0$. Then we aim to find the minimizer of $E(U,c,I)$ in a restricted space

$$\mathscr{A}=\left\{(U,c,I)\,\middle|\,\begin{array}{l}u_i\in\mathrm{BV}(\Omega),\,i=1:N,\,\text{satisfies (i) and (ii)},\,c\in\mathbb{R}^N,\\ I\in\mathrm{BV}(\Omega)\cap L^\infty(\Omega),\,\alpha\leqslant I\leqslant\beta.\end{array}\right\}$$

where the constraint $\alpha\leqslant I\leqslant\beta$ is natural.

DOI: 10.1002/nla

Theorem 2.1
For fixed parameters N, τ, γ, there exists a minimizer of the energy E in the restricted space $\mathscr{A}$.

Proof
It is easy to derive from the Euler–Lagrange equation of energy E that

$$c_i = \frac{\int_\Omega I(x,y)u_i^2(x,y)\,dx\,dy}{\int_\Omega u_i^2(x,y)\,dx\,dy}$$

if $\int_\Omega u_i^2(x,y)\,dx\,dy>0$. If $\int_\Omega u_i^2(x,y)\,dx\,dy=0$ (i.e. $u_i(x,y)=0$ a.e. $(x,y)\in\Omega$), we define $c_i=0$. For such case, the fuzzy membership function is not employed; the number N can be reduced correspondingly.

Now, we can take $I=\alpha, u_i=1/N, c_i=\alpha, i=1:N$, then $E(U,c,I)=(\gamma/2)\int_\Omega(\alpha-I_0)^2\,dx\,dy<+\infty$. Together with the fact that $E\geqslant 0$ in $\mathscr{A}$, we deduce that the infimum of the energy must be finite. To show the existence of a minimizer of the energy, we let $(U^n,c^n,I^n)\subseteq\mathscr{A}$ be a minimizing sequence for energy (7), that is, $E(U^n,c^n,I^n)\to\inf E(U,c,I)$ as $n\to+\infty$. Then there exists a constant $M>0$, such that

$$E(U^n,c^n,I^n)=\int_\Omega|\nabla I^n|\,dx\,dy+\sum_{i=1}^N\int_\Omega|\nabla u_i^n|\,dx\,dy+\frac{\gamma}{2}\int_\Omega(h*I^n-I_0)^2\,dx\,dy$$
$$+\sum_{i=1}^N\frac{\tau}{2}\int_\Omega(I^n-c_i^n)^2(u_i^n)^2\,dx\,dy\leqslant M.$$

Then we have that each term of $E(U^n,c^n,I^n)$ is bounded, i.e.

$$\int_\Omega|\nabla I^n|\,dx\,dy\leqslant M, \tag{8}$$

$$\int_\Omega|\nabla u_i^n|\,dx\,dy\leqslant M, \tag{9}$$

$$\frac{\gamma}{2}\int_\Omega(h*I^n-I_0)^2\,dx\,dy\leqslant M, \tag{10}$$

$$\frac{\tau}{2}\int_\Omega(I^n-c_i^n)^2(u_i^n)^2\,dx\,dy\leqslant M. \tag{11}$$

Since u_i^n satisfies condition (i), $\|u_i^n\|_{L^1(\Omega)}=\int_\Omega u_i^n\,dx\,dy\leqslant|\Omega|$. Together with (9), we get $\{u_i^n\}$ is uniformly bounded in $\mathrm{BV}(\Omega)$ for each $i=1:N$. By the compactness property of BV space, up to a subsequence also denoted by $\{u_i^n\}$ after relabelling, there exists a function $u_i^*\in\mathrm{BV}(\Omega)$ such that

$$u_i^n\to u_i^* \quad \text{strongly in } L^1(\Omega),$$
$$u_i^n\to u_i^* \quad \text{a.e. } (x,y)\in\Omega,$$
$$\nabla u_i^n\rightharpoonup\nabla u_i^* \quad \text{in the sense of measure.}$$

Then by the lower semicontinuity of total variation,

$$\int_\Omega|\nabla u_i^*|\,dx\,dy\leqslant\liminf_{n\to\infty}\int_\Omega|\nabla u_i^n|\,dx\,dy. \tag{12}$$

Meanwhile since u_i^n satisfies constraints (i) and (ii), by the convergence result, u_i^* also satisfies (i) and (ii).

If c_i^n is given by

$$c_i^n=\frac{\int_\Omega I(u_i^n)^2\,dx\,dy}{\int_\Omega(u_i^n)^2\,dx\,dy},$$

DOI: 10.1002/nla

then we have $\alpha \leqslant c_i^n \leqslant \beta$; Otherwise, $c_i^n = 0$. Hence, we get

$$\min(\alpha, 0) \leqslant c_i^n \leqslant \beta.$$

From the boundedness of the sequence $\{c_i^n\}$, we can extract a subsequence, also denoted by $\{c_i^n\}$, and a constant c_i^* such that

$$c_i^n \to c_i^* \quad \text{uniformly.}$$

Since $u_i^n \to u_i^*$, a.e. $(x, y) \in \Omega$ and $c_i^n \to c_i^*$, the Fatou Lemma gives

$$\int_\Omega (I - c_i^*)^2 (u_i^*)^2 \, dx \, dy \leqslant \lim_{n\to\infty} \inf \int_\Omega (I - c_i^n)^2 (u_i^n)^2 \, dx \, dy. \tag{13}$$

The inequality (8) says that the total variation of I^n is uniformly bounded. Since $\alpha \leqslant I^n \leqslant \beta$, we have that the L^1 norm of I^n is uniformly bounded. Then I^n is uniformly bounded in $\mathrm{BV}(\Omega)$, and thus there exists a subsequence $\{I^n\}$ and a function $I^* \in \mathrm{BV}(\Omega)$ and $\alpha \leqslant I^* \leqslant \beta$ such that

$$I^n \to I^* \quad \text{strongly in } L^1(\Omega),$$

$$I^n \to I^* \quad \text{a.e. } (x, y) \in \Omega,$$

$$\nabla I^n \rightharpoonup \nabla I^* \quad \text{in the sense of measure.}$$

Then by the semi-continuity of total variation and L^2 norm, we obtain

$$\int_\Omega |\nabla I^*| \, dx \, dy \leqslant \liminf_{n\to\infty} \int_\Omega |\nabla I^n| \, dx \, dy, \tag{14}$$

$$\int_\Omega (h * I^* - I_0)^2 \, dx \, dy \leqslant \liminf_{n\to\infty} \int_\Omega (h * I^n - I_0)^2 \, dx \, dy. \tag{15}$$

Combining inequalities (12)–(15) for all i, on a suitable subsequence, we have established that

$$E(U^*, c^*, I^*) \leqslant \liminf_{n\to\infty} E(U^n, c^n, I^n) = \inf E(U, c, I) \tag{16}$$

and hence (U^*, c^*, I^*) must be a minimizer. This completes the proof. □

3. THE NUMERICAL METHOD

For efficiency, we choose to follow [14, 19, 20] and use Chambolle's dual projection algorithm [15]. Adding auxiliary variables $V = (v_1, \ldots, v_N)$ and J, we approximate E by

$$E_r(I, J, U, V, c) = \int_\Omega |\nabla J| \, dx + \sum_{i=1}^N \int_\Omega |\nabla v_i| \, dx \, dy + \frac{1}{2\eta} \int_\Omega (I - J)^2 \, dx \, dy + \frac{1}{2\theta} \sum_{i=1}^N \int_\Omega (v_i - u_i)^2 \, dx \, dy$$

$$+ \frac{\gamma}{2} \int_\Omega (h * I - I_0)^2 \, dx \, dy + \sum_{i=1}^N \frac{\tau}{2} \int_\Omega (I - c_i)^2 u_i^2 \, dx \, dy \tag{17}$$

where θ and η are chosen small enough so that I and J, u_i and v_i are almost identical. Since (17) is componentwise convex in each variable I, J, U, V, c, we can minimize it by an alternating method as follows.

3.1. Solve for the vector of constants c

Taking the derivative of E_r with respect to c_i and setting the result to zero, we obtain

$$c_i = \frac{\int_\Omega I(x, y) u_i^2(x, y) \, dx \, dy}{\int_\Omega u_i^2(x, y) \, dx \, dy}. \tag{18}$$

DOI: 10.1002/nla

3.2. Solve for the auxiliary variable V

We solve v_i by minimizing

$$\int_\Omega |\nabla v_i| \, \mathrm{d}x \, \mathrm{d}y + \frac{1}{2\theta} \int_\Omega (v_i - u_i)^2 \, \mathrm{d}x \, \mathrm{d}y.$$

This problem can be efficiently solved by a fast duality projection algorithm. The solution is given by

$$v_i = u_i - \theta \operatorname{div} p_i, \quad i = 1:N, \tag{19}$$

where the vector p_i can be solved by a fixed point method: initializing $p_i^0 = 0$ and iterating

$$p_i^{n+1} = \frac{p_i^n + \phi \nabla(\operatorname{div} p_i^n - u_i/\theta)}{1 + \phi |\nabla(\operatorname{div} p_i^n - u_i/\theta)|}$$

with $\phi \leqslant \frac{1}{8}$ to ensure convergence. See [15] for more details.

3.3. Solve for the membership function U

We consider the minimization problem

$$\min_U \frac{\tau}{2} \sum_{i=1}^N \int_\Omega \mathrm{d}_i u_i^2 \, \mathrm{d}x \, \mathrm{d}y + \frac{1}{2\theta} \sum_{i=1}^N \int_\Omega (v_i - u_i)^2 \, \mathrm{d}x \, \mathrm{d}y \tag{20}$$

subject to constraints (i) and (ii), where $d_i = (I - c_i)^2$ refers to the difference between the denoised/deblurred image and the ith spectral object. In order to give the location of the ith spectral object, the term u_i^2 is used with d_i in the calculation. Since the objective function is strictly convex and the feasible region is convex, there exists a unique global minimizer U^* of problem (20). However, it is hard to get the exact solution [19]. In order to give an approximate numerical solution, first we do not consider the inequality constraints (i). By adding pointwise Lagrange multipliers $\delta(x)$ to handle the equality constraints (ii), we need to minimize

$$\frac{\tau}{2} \sum_{i=1}^N \int_\Omega d_i u_i^2 \, \mathrm{d}x \, \mathrm{d}y + \frac{1}{2\theta} \sum_{i=1}^N \int_\Omega (v_i - u_i)^2 \, \mathrm{d}x \, \mathrm{d}y + \int_\Omega \delta(x) \left(\sum_{i=1}^N u_i - 1 \right) \mathrm{d}x \, \mathrm{d}y.$$

The optimal condition is

$$\tau d_i(x) u_i(x) + \frac{1}{\theta}(u_i(x) - v_i(x)) + \delta(x) = 0.$$

Then the closed-form solution of u_i is given by

$$u_i = \frac{v_i - \theta\delta}{1 + \tau\theta d_i}.$$

Using the constraints $\sum_{i=1}^N u_i = 1$, we have

$$\sum_{i=1}^N \frac{v_i - \theta\delta}{1 + \tau\theta d_i} = 1,$$

then

$$\delta = \frac{\sum_{i=1}^N \dfrac{v_i}{1 + \tau\theta d_i} - 1}{\theta \sum_{i=1}^N \dfrac{1}{1 + \tau\theta d_i}}. \tag{21}$$

DOI: 10.1002/nla

Substituting δ into the formula of u_i gives

$$u_i = \frac{v_i}{1+\tau\theta d_i} - \frac{\sum_{j=1}^{N} \frac{v_j}{1+\tau\theta d_j} - 1}{\sum_{j=1}^{N} \frac{1+\tau\theta d_i}{1+\tau\theta d_j}}.$$

Second, we can apply the inequality constraints by projecting u_i onto $[0, 1]$,

$$\hat{u}_i := \min\{\max\{u_i, 0\}, 1\}. \tag{22}$$

Finally, $\hat{u}_i$ gives our approximate numerical solution.

3.4. Solve for the auxiliary variable J

J can be solved by minimizing

$$\int_\Omega |\nabla J| \, dx \, dy + \frac{1}{2\eta} \int_\Omega (I-J)^2 \, dx \, dy$$

Using the fast dual projection method as in Section 3.2, the solution is given by

$$J = I - \eta \operatorname{div} p, \tag{23}$$

where the vector p can be determined by a fixed point method. See Section 3.2 for details.

3.5. Solve for I

Taking the derivative of E_r with respect to I and setting the result to zero, we obtain

$$\frac{\delta E_r}{\delta I} = \frac{1}{\eta}(I-J) + \gamma h^{-1} * (h * I - I_0) + \tau \sum_{i=1}^{N} (I - c_i) u_i^2 = 0.$$

Then I can be determined by

$$I = \mathscr{F}^{-1}\left(\frac{\mathscr{F}(J) + \gamma\eta \mathscr{F}(h)^* \circ \mathscr{F}(I_0) + \tau\eta \sum_{i=1}^{N} (c_i \mathscr{F}(u_i)^2)}{1 + \gamma\eta \mathscr{F}(h)^* \circ \mathscr{F}(h) + \tau\eta \sum_{i=1}^{N} (\mathscr{F}(u_i)^2)} \right), \tag{24}$$

where $\mathscr{F}$ denotes the Fourier transform.

We remark that in the deblurring process, the parameter η is chosen to be a sequence that goes to zero. In fact, we choose the initial value of η to 0.1 and then decrease it by $\eta = \eta/1.2$ during the evolution. The factor 1.2 is chosen following [16] in which it is got by trail and error when considering the deblurred image quality. The evolution of I, J is stopped when $\eta < 1\text{e}-8$.

3.6. Algorithm details

The algorithm for minimizing E_r in (17) can be summarized in the following six steps:

- *Step 1*. Initialize the membership functions u_i such that the constraints (i) and (ii) are both satisfied. Set $I = I_0$, $J = I$, $v_i = u_i$, $\eta = 0.1$.
- *Step 2*. Calculate c_i by formula (18).
- *Step 3*. Update v_i by formula (19).
- *Step 4*. Update the membership functions u_i using formula (22).
  Set $\eta = \eta/1.2$.
- *Step 5*. Update J by formula (23).
- *Step 6*. Update I by formula (24).
  If $\eta < 1\text{e}-8$, end steps 5 and 6.

DOI: 10.1002/nla

Repeat Steps 2–6 until termination. The termination criterion is as follows:

$$\|c^{k+1}-c^k\|\leqslant\varepsilon,$$

where $c^k=(c_1^k,\ldots,c_N^k)$ is the vector of intensity values of N spectral objects in the kth iteration and $\|\cdot\|$ denotes the Euclidean distance and ε is a small positive number defined by the user.

3.7. *Extending the algorithm to hyperspectral image data*

In this subsection, we present the extension of our algorithm to three-dimensional tensors, specifically hyperspectral data cubes. Let $I(x,y,\lambda):\Omega\times\mathscr{W}\to\mathbb{R}$ denote the tensor image where x and y denote spatial variables and λ is the spectral variable. In the discrete form, we can view I as a vector-valued image as follows: $I=(I_1,\ldots,I_m):\Omega\to\mathbb{R}^m$. Here m is the number of spectral frequencies (wavelengths in spectral terminology) to be considered. Then the piecewise constant image model changes to

$$I_j(x,y)\approx c_{ij},\quad j=1:m\quad(x,y)\in\Omega_i$$

where $\{\Omega_i\}_{i=1}^N$ is a partition of the image domain Ω, and $c_i=(c_{i1},\ldots,c_{im})$ is a spectral vector of the ith object (or the spectrum of the ith object). Then we can formulate a matrix $C=[c_{ij}]$, which denotes the spectral traces of all the segmented objects in the hyperspectral data cube. Note that these spectral traces, sometimes called endmembers, are determined here without matching with a spectral library as is often used, e.g. [21].

Similarly, consider the matrix $U=(u_1,\ldots,u_N)$. The rows $u_i(x,y)$ of U represent the hard membership functions χ_i in (4), and must satisfy (5).

Denote the observed hyperspectral tensor by I_0. We combine the denoising/deblurring model and the fuzzy piecewise constant segmentation model together with $p=2$, and consider a coupled model for denoising/deblurring and segmentation, which has to minimize

$$E(U,C,I)=\sum_{j=1}^m\int_\Omega|\nabla I_j|\,\mathrm{d}x\,\mathrm{d}y+\sum_{i=1}^N\int_\Omega|\nabla u_i|\,\mathrm{d}x\,\mathrm{d}y+\frac{\gamma}{2}\int_\Omega(h*I-I_0)^2\,\mathrm{d}x\,\mathrm{d}y$$
$$+\sum_{i=1}^N\frac{\tau}{2}\int_\Omega\frac{1}{m}\sum_{j=1}^m(I_j-c_{ij})^2u_i^2\,\mathrm{d}x\,\mathrm{d}y,\tag{25}$$

subject to constraints (i) and (ii) in (5). Here $d_{ij}=(I_j-c_{ij})^2$ refers to the the difference in the jth spectral band between the denoised/deblurred tensor image and the ith spectral object. We can set the difference between the denoised/deblurred tensor image and the ith spectral object to be the average of the m spectral bands:

$$d_i=\frac{d_{i1}+\cdots+d_{im}}{m}.$$

In order to give the location of the ith spectral object, the term u_i^2 is used with d_i in the calculation. The algorithm in the previous subsection can now be employed to the hyperspectral tensor case. For example, it is easy to obtain the new formulas for the components of the matrix C, i.e.

$$c_{ij}=\frac{\int_\Omega I_ju_i^2\,\mathrm{d}x\,\mathrm{d}y}{\int_\Omega u_i^2\,\mathrm{d}x\,\mathrm{d}y}.$$

Then the formulas for I_i, J_i are similar to I, J in the grayscale image case. The unknowns can be updated similarly according to the procedures in Algorithm 1.

Here we would like to remark that similarly to a tensor decomposition of I, we can also interpret our decomposition of I by using the compressive representation matrices U and C as follows:

$$I(x,y,j)=\sum_{i=1}^N u_i(x,y)c_{ij}\quad\forall(x,y)\quad\text{and}\quad1\leqslant j\leqslant m.$$

DOI: 10.1002/nla

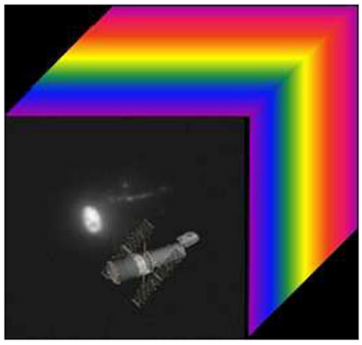

Figure 1. The original simulated image of the Hubble Space Telescope [11], representative of the data collected by the Maui ASIS system.

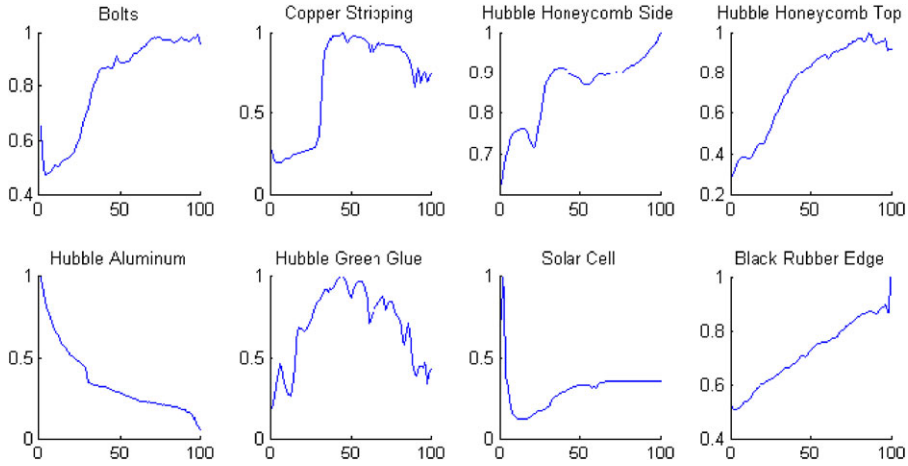

Figure 2. Spectral signatures of eight materials assigned to simulated Hubble Space Telescope model.

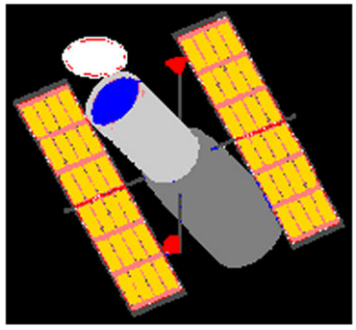

Figure 3. Materials assigned to pixels in Hubble Satellite Telescope image.

4. HYPERSPECTRAL DATA SET SIMULATING SPACE OBSERVATIONS

For safety and other considerations in space, nonresolved space object characterization is an important component of space situational awareness (SSA). The key problem in nonresolved space object characterization is to use spectral reflectance data to gain knowledge regarding the physical properties (e.g. function, size, type, status change) of space objects that cannot be spatially resolved with normal panchromatic telescope technology. Such objects may include geosynchronous

DOI: 10.1002/nla

Table I. Materials, colors and fractional abundances used for the Hubble satellite simulation.

Material	Color	Fractional abundance (%)
Bolts	Red	3
Copper stripping	Cyan	13
Hubble honeycomb side	Blue	3
Hubble honeycomb top	White	4
Hubble aluminum	Light gray	19
Hubble green glue	Dark gray	12
Solar cell	Gold	37
Black rubber edge	Dark gray	8

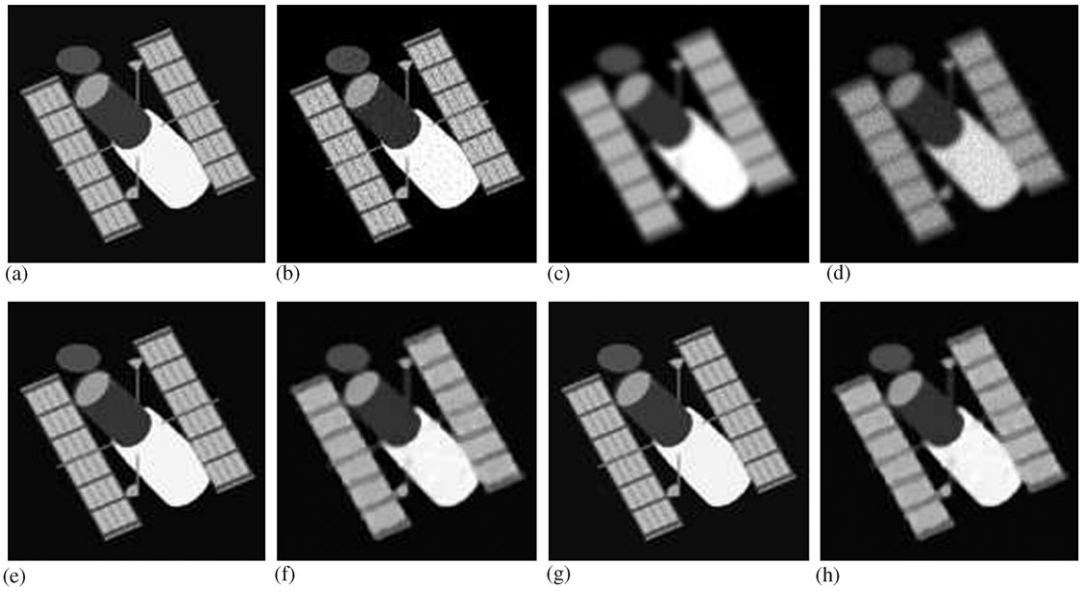

Figure 4. Band 1 of the hyperspectral tensor image: (a) the original clean image; (b) image with noise; (c) image with blur; (d) image with blur and noise; (e) deblurred image for (c) with our fast denoising/deblurring algorithm; (f) deblurred image for (d) with our fast denoising/deblurring algorithm; (g) deblurred image with coupled segmentation and deblurring algorithm for (c); and (h) deblurred image with coupled segmentation and deblurring algorithm for (d).

satellites, rocket bodies, platforms, space debris or nano-satellites. Spectral reflectance data of a space object can be gathered using ground-based spectrometers, such as the SPICA system, see [22–24], located on the 1.6-m Gemini telescope and the ASIS system, see [5, 11, 12], located on the 3.67-m telescope at the Maui Space Surveillance Complex (MSSC), and contains essential information regarding the makeup or types of materials comprising the object. Different materials, such as aluminum, mylar, paint, plastics and solar cell, possess fairly unique characteristic wavelength-dependent absorption features, or spectral *signatures*, which mix together in the spectral reflectance measurement of an object.

Spectral unmixing is a problem that originated within the hyperspectral imaging community and several computational methods to solve it have been proposed over the last few years. A thorough study and comparison of various computational methods for endmember or spectral signature computation, in the related context of hyperspectral unmixing, can be found in the work of Plaza *et al.* [25]. An information-theoretic approach has been provided by Wang and Chang [8].

In an earlier project on spectral data analysis for SOI, some of the authors have employed NMF algorithms for unmixing of spectral reflectance data from a single pixel imaged by the SPICA

DOI: 10.1002/nla

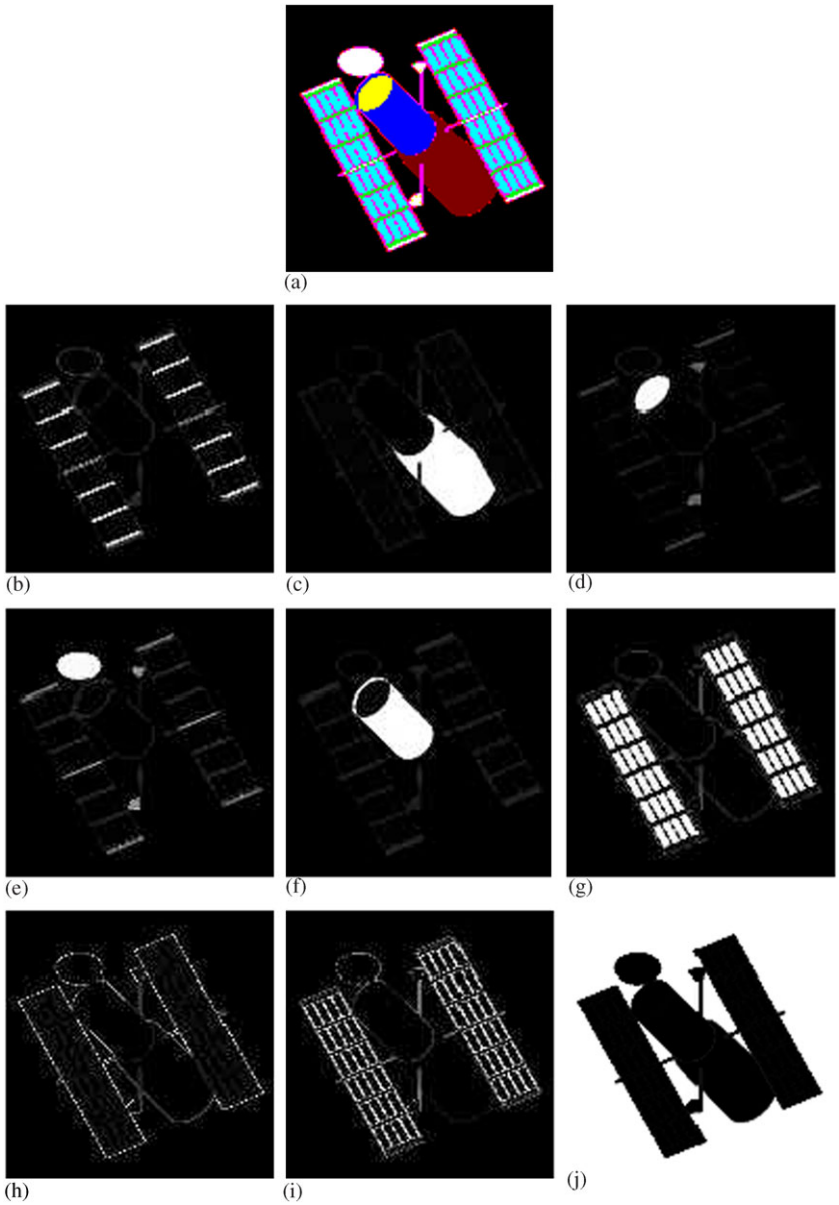

Figure 5. Segmentation of the clean tensor image: (a) the segmentation result and (b)–(j) the membership functions u_1 to u_9.

spectrometer at MCSS to find endmember candidates. In that work, regularized inverse problem methods for determining corresponding fractional abundances were developed [23, 24].

A new spectral imaging sensor, capable of collecting hyperspectral images of space objects, has been installed on the 3.67-m Advanced Electrocal-Optical System (AEOS) at the MSSC. The AEOS Spectral Imaging Sensor (ASIS) is used to collect adaptive optics-compensated spectral images of astronomical objects and satellites. In a series of papers, Blake *et al.* [5, 11, 12] have developed model-based spectral image deconvolution methods that can simultaneously remove some of the spatial and imaging system-caused spectral blurring introduced by the ASIS sensor. See Figure 1 for a simulated hyperspectral image of the Hubble Space Telescope from [11], similar to that collected by ASIS.

DOI: 10.1002/nla

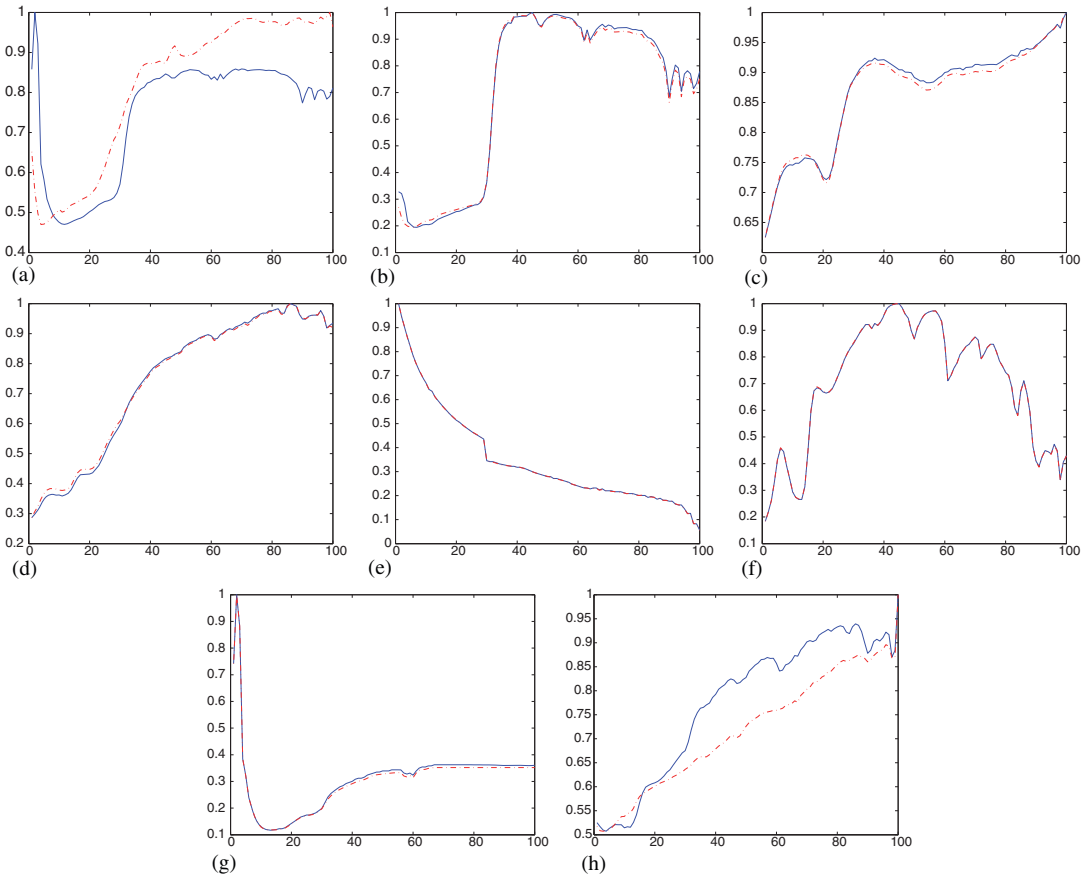

Figure 6. (The clean tensor image) The original material spectral signatures: red and -. and the estimated spectral signatures: blue and – : (a) bolts; (b) copper stripping; (c) Hubble honeycomb side; (d) Hubble honeycomb top; (e) Hubble aluminum; (f) Hubble green glue; (g) solar cell; and (h) black rubber edge.

For our numerical tests, we use the data developed by Zhang *et al.* in [2], where the authors constructed a data set of simulated spectral data using a 3-D model of the Hubble Space Telescope and an NASA library of material spectral signatures [26]. These are lab-measured reflectance ratios obtained by comparing the measured reflectance of each material to a known reflectance of a white reference. The 3-D model was discretized into a 128×128 array of pixels for which a specific mixture of eight materials was assigned based on orientation of the Hubble telescope. Figure 2 shows the spectral signatures of these materials. The signatures cover a band of spectrum from 0.4 to 2.5 μm for 100 evenly distributed sampling points, leading to a hyperspectral data cube, or 3D tensor, $\mathscr{T}_0$, of size $128 \times 128 \times 100$.

Three other hyperspectral (3D tensor) data sets, $\mathscr{T}_1$, $\mathscr{T}_2$, and $\mathscr{T}_3$, were then constructed from the $\mathscr{T}_0$ by considering: (i) spatial blur (Gaussian psf with standard deviation of 2 pixels), (ii) noise (independent Gaussian and signal-dependent Poisson noise associated with the light detection process) and (iii) a mixture of blur and noise. We simulate the practical situations of observing hyperspectral data in a simple way, i.e. to simulate the optical blurring with a Gaussian PSF and the various noises present in the atmosphere and in the imaging system with a noise model. These simplifications can easily be replaced by for example, more advanced turbulence models, for future studies. We adopt a widely used noise model [27] for modifying our tensor $\mathscr{T}$ to $\tilde{\mathscr{T}}$, specified by

$$\tilde{t}_{ijk} = t_{ijk} + n^{(1)}_{ijk}\sqrt{t_{ijk}} + n^{(2)}_{ijk}, \tag{26}$$

DOI: 10.1002/nla

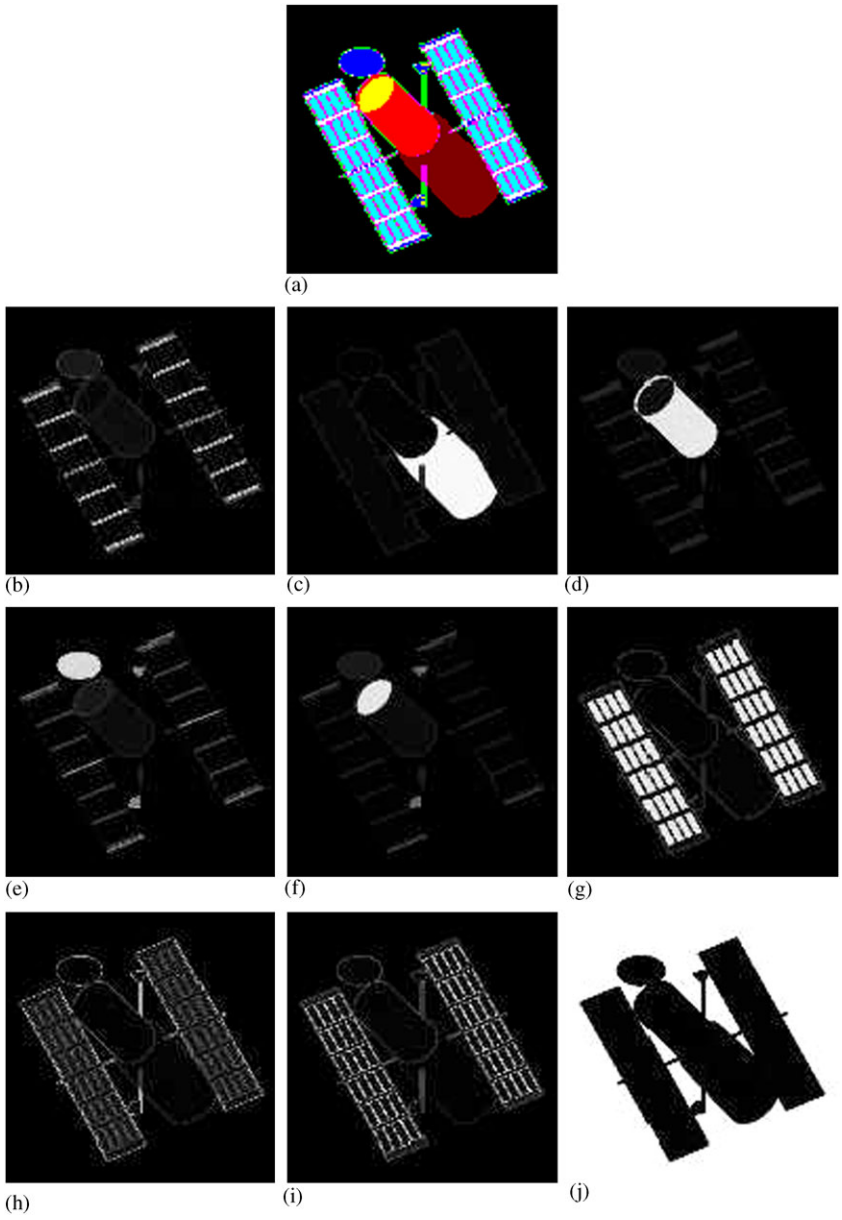

Figure 7. Segmentation of the noisy tensor image using the coupled segmentation and denoising/deblurring algorithm; (a) the segmentation result and (b)–(j) the membership functions u_1 to u_9.

where $n^{(1)} \in N(0, \sigma_1)$ and $n^{(2)} \in N(0, \sigma_2)$. Here we set $\sigma_1 = 0.05$ and $\sigma_2 = 0.005$.

As an illustration of original material signatures assigned to each image pixel, we render an image of Hubble Space Telescope, Figure 3, using the color map defined in Table I.

5. EXPERIMENTAL RESULTS

We test our algorithm on the four hyperspectral tensor images with size $128 \times 128 \times 100$: the original clear image, the noisy image, the blurred image, the blurred and noisy image. In the first row of Figure 4, the first band of the tensor image is shown. The second row shows the deblurred

DOI: 10.1002/nla

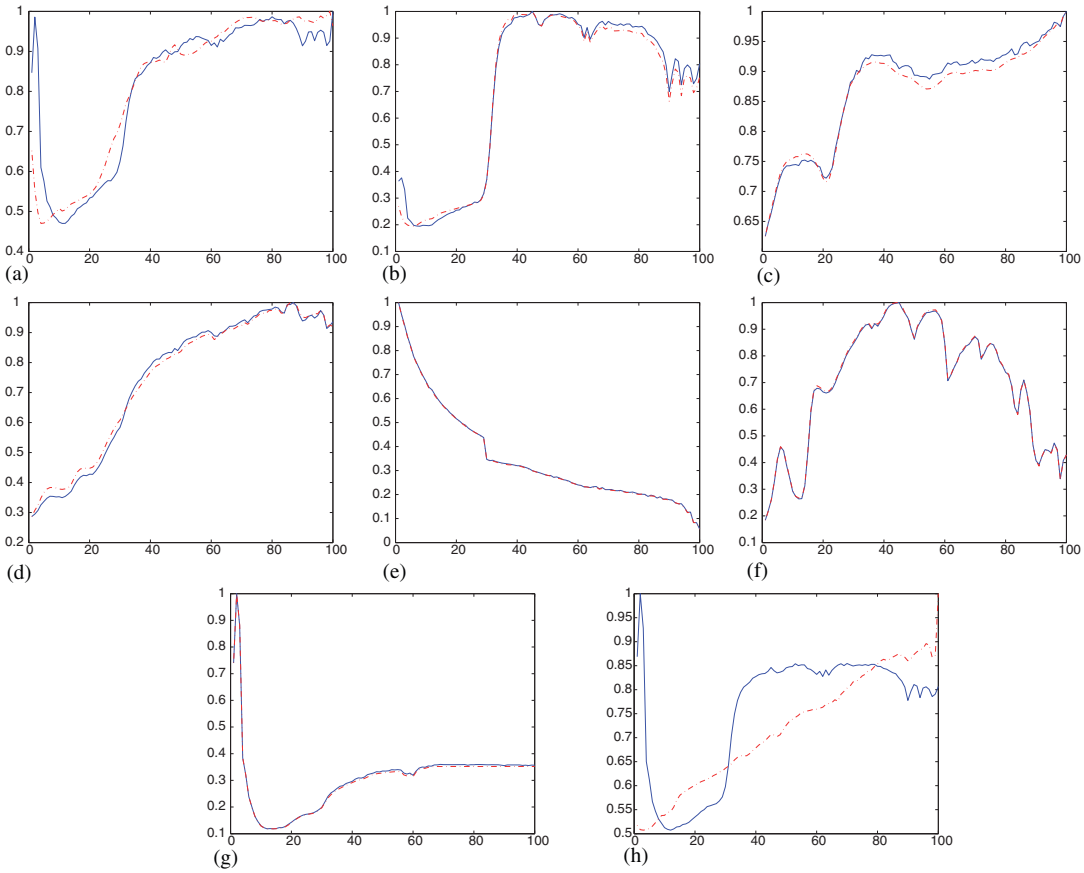

Figure 8. (The noisy tensor image) The original material spectral signatures: red and -. and the estimated spectral signatures: blue and – : (a) bolts; (b) copper stripping; (c) Hubble honeycomb side; (d) Hubble honeycomb top; (e) Hubble aluminum; (f) Hubble green glue; (g) solar cell; and (h) black rubber edge.

image using the fast denoising/deblurring model and our coupled model. It is clear that our coupled model has a similar performance as the denoising/deblurring model in the aspect of deblurring. In Figures 5–12, we test the four tensor images. We set $N=9$ and give the segmentation results and the nine membership functions (including the background) in Figures 5, 7, 9 and 11. For instance, in Figure 5(a), the segmentation result refers to different regions based on the matrix U. In Figures 5(b)–(j), we show the values of the membership functions u_i except the background. When the pixel intensity is white in the figures, this indicates that this pixel belongs to a particular region in an image. Similarly, when the pixel intensity is black in the figures, this indicates that this pixel does not belong to the region formed. There may be some gray pixel intensities, which indicates that the pixel may or may not belong to the segmented region. As is usual, we choose the maximal value among all the membership functions to decide to which region this pixel belongs.

In Figures 6, 8, 10 and 12, we show the original spectral signatures and the estimated spectral signatures for the membership functions. In these figures, the values of c_{ij} are shown with respect to region i of an image. In the clean and blurred tensor images, we find in Figures 6 and 10 that the estimated spectral signatures for Bolts and Black Rubber Edge are not matched well with the original spectral signatures. The reason is that they are the smaller and thinner parts: they get mixed with surrounding materials, which make them difficult to extract. However, the proposed method estimates the other materials very well.

DOI: 10.1002/nla

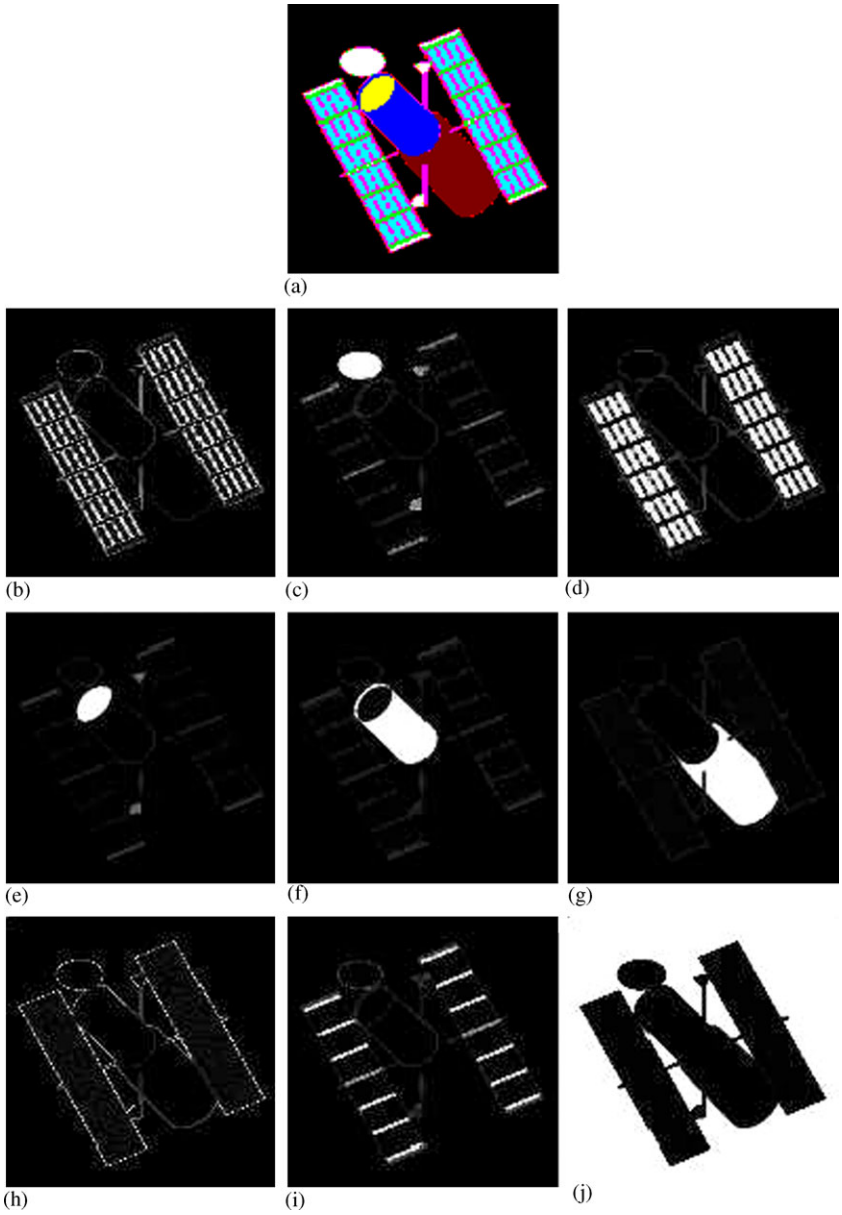

Figure 9. Segmentation of the blurred tensor image with the coupled segmentation and denoising/deblurring algorithm: (a) the segmentation result and (b)–(j) the membership functions u_1 to u_9.

In the noisy image, the estimated spectral vectors are matched with the original spectral vectors except the Black Rubber Edge, see Figure 8. In the blurred and noisy tensor image, there are three materials (Bolts, Honeycomb Side and Black Rubber Edge) that are not matched very well, but the estimated spectral signatures of the other materials are quite good. We observe in these figures that there are some channels of the spectral signatures (Copper Stripping, Hubble Honeycomb Top, Hubble Aluminum, Hubble Green Glue and Solar Cell) that are estimated consistently well in the four situations: the clear image, the denoised image, the deblurred image and the deblurred and denoised image.

Table II demonstrates the computational times and the iterations of the proposed algorithm with respect to the clean tensor image, the noisy tensor image, the blurred tensor image, the blurred and noisy tensor image, respectively. It shows that our algorithm is quite efficient.

DOI: 10.1002/nla

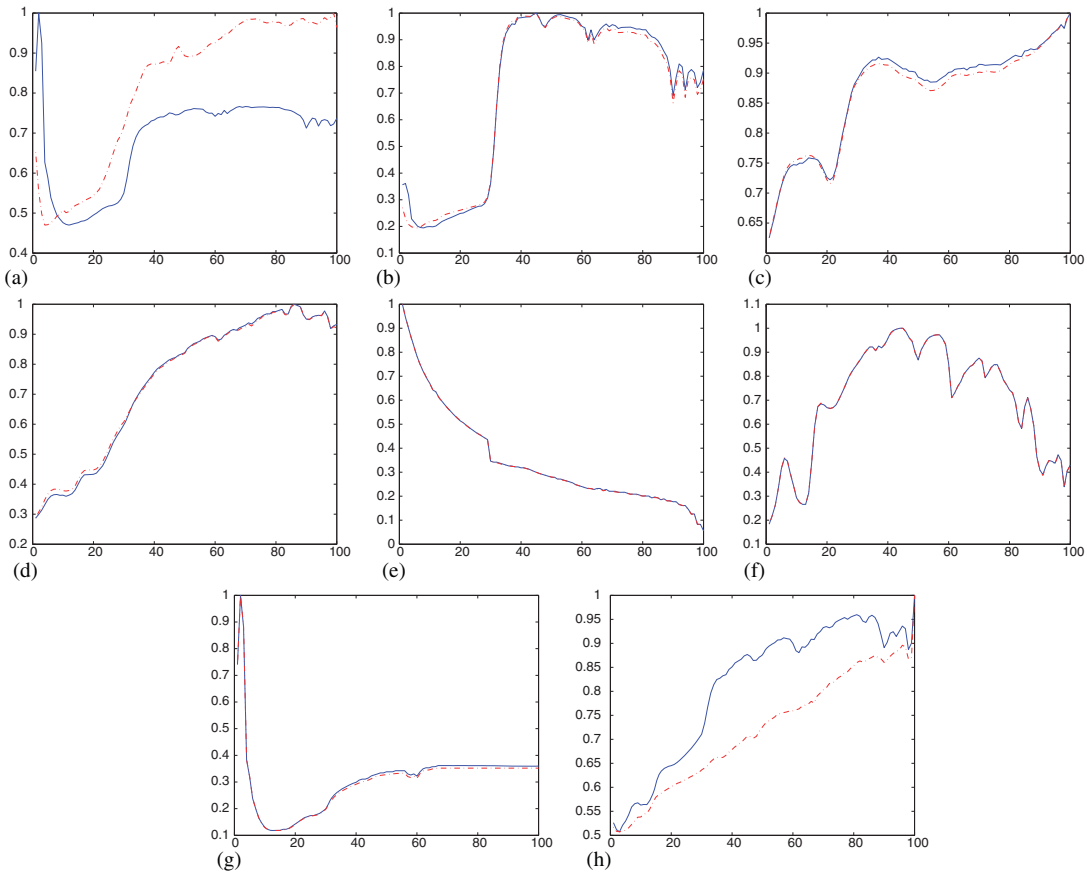

Figure 10. (The blurred tensor image) The original material spectral signatures: red and -. and the estimated spectral signatures: blue and – : (a) bolts; (b) copper stripping; (c) Hubble honeycomb side; (d) Hubble honeycomb top; (e) Hubble aluminum; (f) Hubble green glue; (g) solar cell; and (h) black rubber edge.

6. CONCLUSIONS AND FUTURE WORK

In this paper, we have developed a combined variational image restoration and segmentation model for hyperspectral space object unsupervised material identification in the presence of noise and blur. Mathematically, the existence of a solution to the proposed energy functional minimization is proved in a restricted space. Numerically, the model is solved by a convergent alternating minimization method. We add new variables in the energy functional so that two of the subproblems can be solved by fast dual projection methods. The model provides the segmentation result and the restored image simultaneously. Numerical results show that our proposed method is a promising approach to hyperspectral material identification associated with SOI.

Although experimentally the combined algorithm is fast and gives quite good results, the theoretical proof of the convergence of the algorithm is important. To improve the solution for the smaller and thinner parts, one possible way is to put more weights on these parts. These will be studied in future work.

In future work, comparisons of our variational method will be made with the recent development of multilevel iterative methods for deblurring, denoising and segmentation by Morigi *et al.* [28]. It will be interesting to compare the overall effectiveness and computational efforts of these related approaches, using an extension of their method to hyperspectral data.

Another, rather different, approach to obtaining compressive representation of hyperspectral data has been recently investigated by Gillis and Plemmons [29], who propose the use of matrix

DOI: 10.1002/nla

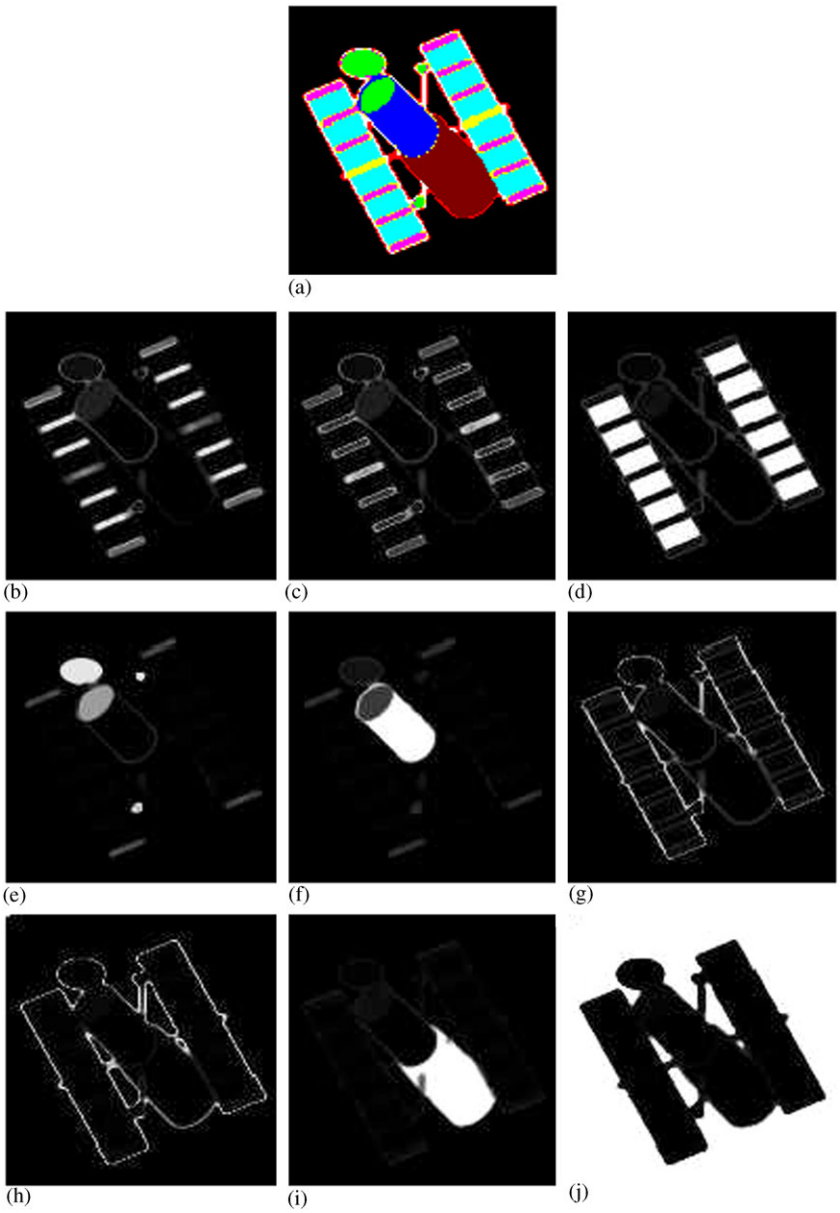

Figure 11. Segmentation of the blurred and noisy tensor image with the coupled segmentation and denoising/deblurring algorithm: (a) the segmentation result and (b)–(j) the membership functions u_1 to u_9.

and tensor factorization methods in the spirit of PCA. NMF and its variants have recently been successfully used as dimensionality reduction techniques for identification of the materials present in hyperspectral images. In their paper, the authors present a new variant of NMF called nonnegative matrix underapproximation (NMU), based on the introduction of underapproximation constraints which enables one to extract features in a recursive way, like PCA, but preserving nonnegativity. These additional constraints appear to make NMU particularly well-suited to achieve a parts-based and sparse representation of the data, enabling it to recover the constitutive elements in hyperspectral data. A comparison between our methods proposed here and the methods in [29] in terms of compressive representation capabilities on a variety of hyperspectral data cubes is given here.

DOI: 10.1002/nla

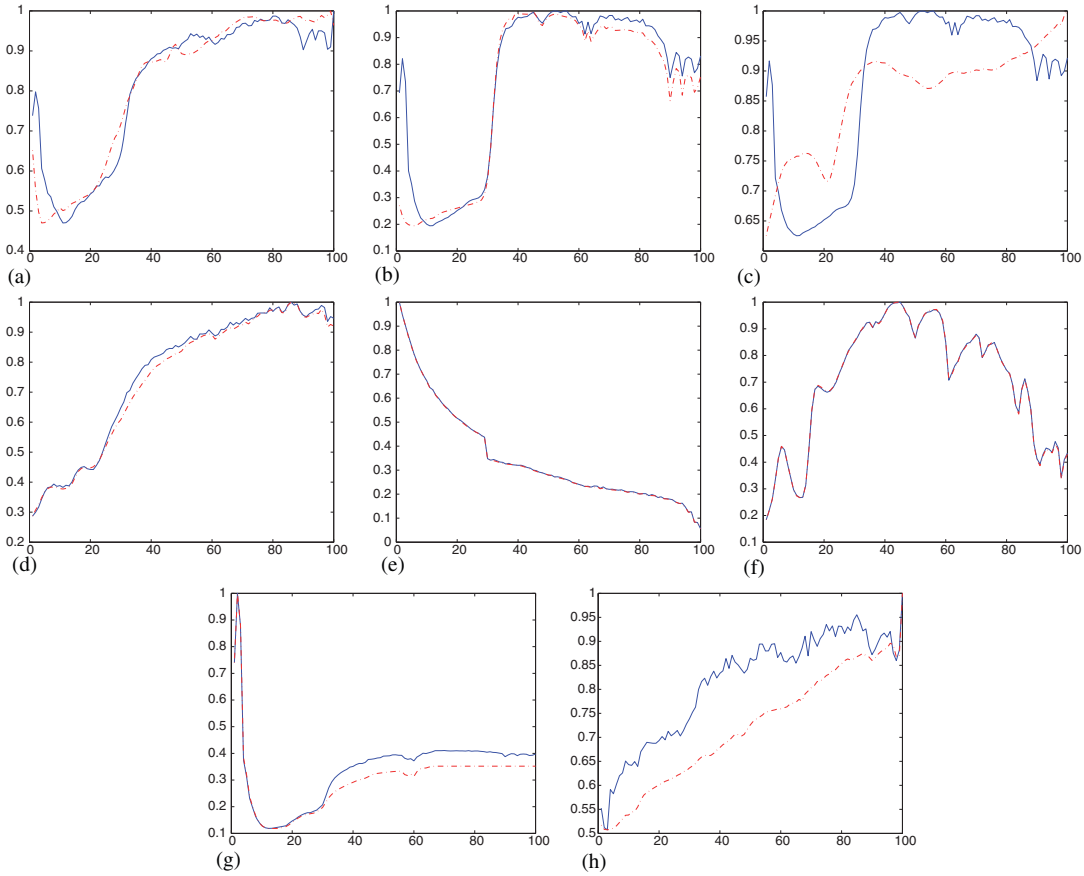

Figure 12. (The blurred and noisy tensor image) The original material spectral signatures: red and -. and the estimated spectral signatures: blue and – : (a) bolts; (b) copper stripping; (c) Hubble honeycomb side; (d) Hubble honeycomb top; (e) Hubble aluminum; (f) Hubble green glue; (g) solar cell; and (h) black rubber edge.

Table II. The computational cost of the proposed algorithm.

Tensor image	Iterations	Computational time (s)
Clean	27	22.3
Noisy	38	35.5
Blurred	64	126.9
Blurred and noisy	48	117.0

Future work also includes refinement of our combined deblurring, denoising and segmentation model to include supervised learning (classification) capabilities. We are interested in applying our method to analyze remote sensing hyperspectral data obtained from airborne imagery for studying ecological conditions and changes, as the work of Goodwin *et al.* [30] and the work of Saatchi *et al.* [31].

Testing will also be made on geospatial hyperspectral data obtained from the Army Geospatial Center. This will include the HYDICE data cubes Urban and Terrain,[‡] considered recently by Guo [21].

[‡]Available at *http://www.agc.army.mil/hypercube/.*

DOI: 10.1002/nla

ACKNOWLEDGEMENTS

The authors would like to thank the reviewers for their very helpful comments and suggestions. We would also like to thank Sudhakar Prasad and Peter Zhang for their interaction during the preparation of the manuscript. This research was supported in part by the National Science Foundation of Shanghai (10ZR1410200), the National Science Foundation of China (60773119), HKRGC (201508), HKBU FRGs and the U.S. Air Force Office of Scientific Research (AFOSR), with award number FA9550-08-1-0151.

REFERENCES

1. Van Loan C. Future directions in tensor-based computation and modeling, 2009. Available at: http://www.cs.cornell.edu/cv/TenWork/FinalReport.pdf.
2. Zhang Q, Wang H, Plemmons R, Pauca P. Tensor methods for hyperspectral data analysis: a space object material identification study. *Journal of the Optical Society of America, A* 2008; **25**(12):3001–3012.
3. Kolda TG, Bader BW. Tensor decompositions and applications. *SIAM Review* 2009; **51**(3):455–500.
4. Chen D, Plemmons R. Nonnegativity constraints in numerical analysis. In *The Birth of Numerical Analysis*, Bultheel A, Cools R (eds). World Scientific Press: Singapore, 2009.
5. Blake T, Cain S, Goda M, Jerkatis K. Enhancing the resolution of spectral images. *Proceedings of SPIE* 2006; **6233**:623309.
6. Du Y, Chang C-I, Ren H, Chang C-C, Jensen JO, D'Amico FM. New hyperspectral discrimination measure for spectral characterization. *Optical Engineering* 2004; **43**:1777–1786.
7. Hege K, O'Connell D, Johnson W, Basty S, Dereniak E. Hyperspectral imaging for astronomy and space surveillance. In *Imaging Spectrometry IX*, Chen SS, Lewis PE (eds). SPIE: Bellingham, WA; *Proceedings of SPIE* 2003; **5159**:380–391.
8. Wang J, Chang C-I. Applications of independent component analysis (ICA) in endmember extraction and abundance quantification for hyperspectral imagery. *IEEE Transactions on Geoscience and Remote Sensing* 2006; **44**:2601–2616.
9. Chan TF, Vese LA. Active contour without edges. *IEEE Transactions on Image Processing* 2001; **10**:266–277.
10. Pi L, Shen C, Li F, Fan J. A variational formulation of segmenting desired objects in color images. *Image and Vision Computing* 2007; **25**:1414–1421.
11. Blake T, Cain S, Goda M, Jerkatis K. Model of the AEOS spectral imaging sensor (ASIS) for spectral image deconvolution. *Proceedings of AMOS Technical Conference*, Maui, 2005.
12. Blake T, Cain S, Goda M, Jerkatis K. Reconstruction of spectral images from the AEOS spectral imaging sensor. *Proceedings of AMOS Technical Conference*, Maui, 2006.
13. Roggemann MC, Welsh B. *Imaging Through Turbulence*. CRC Press: Boca Raton, 1996.
14. Huang Y, Ng M, Wen Y. A fast total variation minimization method for image restoration. *SIAM Journal on Multiscale Modeling and Simulation* 2008; **7**:774–795.
15. Chambolle A. An algorithm for total variation minimization and applications. *Journal of Mathematical Imaging and Vision* 2004; **20**(1–2):89–97.
16. Liao H, Li F, Ng MK. Generalized cross-validation for total variation image restoration. *Journal of the Optical Society of America, A* 2009; **26**:2311–2320.
17. Mumford D, Shah J. Optimal approximations by piecewise smooth functions and associated variational problems. *Communications on Pure and Applied Mathematics* 1989; **42**:577–685.
18. Ahmed MN, Yamany SM, Mohamed N, Farag AA, Moriarty T. A modified fuzzy C-means algorithm for bias field estimation and segmentation of MRI data. *IEEE Transactions on Medical Imaging* 2002; **21**(3):193–199.
19. Mory B, Ardon R. Fuzzy region competition: a convex two-phase segmentation framework. In *SSVM 2007*, Sgallari F, Murli A, Paragios N (eds). Lecture Notes in Computer Science, vol. 4485. Springer: Berlin, 2007; 214–226.
20. Bresson X, Esedoglu S, Vandergheynst P, Thiran J-P, Osher S. Fast global minimization of the active contour/snake model. *Journal of Mathematical Imaging and Vision* 2007; **28**(2):151–167.
21. Guo Z, Wittman T, Osher S. ℓ_1 unmixing and its application to hyperspectral image enhancement. In *Algorithms and Technologies for Multispectral, Hyperspectral, and Ultraspectral Imagery XV*, Shen S, Lewis P (eds). SPIE: Bellingham, WA; *Proceedings of the SPIE* 2009; **7334**:73341M–73341M-9.
22. Abercromby K, Africano J, Hamada K, Stansbery E, Sydney P, Kervin P. Physical properties of orbital debris from spectroscopic observations. *Advances in Space Research* 2004; **34**:1021–1025.
23. Pauca P, Piper J, Plemmons R. Nonnegative matrix factorization for spectral data analysis. *Linear Algebra and its Applications* 2006; **416**:29–47.
24. Pauca P, Piper J, Plemmons R, Giffin M. Object characterization from spectral data using nonnegative factorization and information theory. *Proceedings of AMOS Technical Conference*, Maui, 2004.
25. Plaza A, Martinez P, Perez R, Plaza J. Spatial/spectral endmember extraction by multidimensional morphological operations. *IEEE Transactions on Geoscience and Remote Sensing* 2002; **40**:2025–2041.
26. Abercromby K. NASA Johnson Space Center, personal communication, 2006.
27. Jain AK. *Fundamentals of Digital Image Processing*. Prentice-Hall: Englewood Cliffs, NJ, 1989.

DOI: 10.1002/nla

28. Morigi1 S, Reichel L, Sgallari F. An edge-preserving multilevel method for deblurring, denoising, and segmentation. In *Scale Space and Variational Methods in Computer Vision*, Tai X-C, Morken K, Lysaker M, Lie K-A (eds). Lecture Notes in Computer Science, vol. 5567. Springer: Berlin, 2009; 427–438.
29. Gillis N, Plemmons R. Dimensionality reduction, classification, and spectral mixture analysis using nonnegative underapproximation. *Proceedings of the SPIE Conference on Defense*, *Security and Sensing*, Orlando, 2010. Available at: http://www.wfu.edu/∼plemmons.
30. Goodwin N, Coops NC, Stone C. Assessing plantation canopy condition from airborne imagery using spectral mixture analysis and fractional abundances. *International Journal of Applied Earth Observation and Geoinformation* 2005; **7**:11–28.
31. Saatchi S, Buermann W, Mori S, Ter Steege H. Modeling distribution of ama- zonian tree species and diversity using remote sensing measurements. *Remote Sensing of Environment* 2008; **112**:2000–2017.

DOI: 10.1002/nla